

SpectralTrain: A Universal Framework for Hyperspectral Image Classification

Meihua Zhou¹, Liping Yu¹, Jiawei Cai², Wai Kin Fung³,
Ruiguo Hu⁴, Jiarui Zhao¹, Wenzhuo Liu⁵, Nan Wan^{6*}

¹University of Chinese Academy of Sciences, Beijing, China.

²School of Earth and Space Sciences, Peking University, Beijing, China.

³The Chinese University of Hong Kong, Hong Kong, China.

⁴Northeastern University, Liaoning, China.

⁵Faculty of Marine Science and Technology, Beijing Institute of Technology, Zhuhai, China.

⁶School of Medical Information, Wannan Medical University, Wuhu, China.

*Corresponding author(s). E-mail(s): wannan@wnmc.edu.cn;

Contributing authors: mzhou0412@gmail.com,

zhoumeihua25@mails.ucas.ac.cn; ylp1992247079@gmail.com;

cjw2403878745@163.com; 1155208542@link.cuhk.edu.hk;

hrg010923@163.com; zhaojiarui@binn.cas.cn; wzliu@bit.edu.cn;

Abstract

Hyperspectral image (HSI) classification typically involves large-scale data and computationally intensive training, which limits the practical deployment of deep learning models in real-world remote sensing tasks. This study introduces SpectralTrain, a universal, architecture-agnostic training framework that enhances learning efficiency by integrating curriculum learning (CL) with principal component analysis (PCA)-based spectral downsampling. By gradually introducing spectral complexity while preserving essential information, SpectralTrain enables efficient learning of spectral – spatial patterns at significantly reduced computational costs. The framework is independent of specific architectures, optimizers, or loss functions and is compatible with both classical and state-of-the-art (SOTA) models. Extensive experiments on three benchmark datasets — Indian Pines, Salinas-A, and the newly introduced CloudPatch-7 — demonstrate strong generalization across spatial scales, spectral characteristics,

and application domains. The results indicate consistent reductions in training time by $2\text{--}7\times$ speedups with small-to-moderate accuracy deltas depending on backbone. Its application to cloud classification further reveals potential in climate-related remote sensing, emphasizing training strategy optimization as an effective complement to architectural design in HSI models. Code is available at <https://github.com/mh-zhou/SpectralTrain>.

Keywords: Hyperspectral image classification, Curriculum learning, Efficient training, Cloud spotting, Climate applications

1 Introduction

Hyperspectral imaging (HSI) provides densely sampled spectra per pixel over hundreds of contiguous bands, enabling fine-grained material discrimination across agriculture, Earth observation, and atmosphere-related applications [1–3]. Beyond generic high dimensionality, HSI exhibits domain-specific factors that make efficient training uniquely challenging for *classification*: (i) band-localized cues: class-discriminative information often concentrates in narrow, non-uniform wavelength intervals, so uniform downsampling or early heavy compression can remove task-relevant signals; (ii) spectral ordering and sensing topology: random or frequency-only truncation ignores the contiguous, instrument-induced structure of HSI cubes, causing spectral aliasing and unstable early gradients; (iii) cross-sensor spectral response and domain shift: fixed efficiency schedules tuned for one instrument may not transfer across sensors; and (iv) bandwidth-bound pipelines: compute and data movement scale with the number of bands, so starting from full spectra wastes early-epoch compute before coarse separations are learned [4, 5]. These HSI-specific properties explain why efficiency recipes devised for RGB (e.g., frequency truncation, uniform band dropping) are especially insufficient when naively transplanted to HSI classification [6, 7].

Motivated by EfficientTrain++ [8], we revisit efficiency from a training-*schedule* perspective rather than architectural changes. To the best of our knowledge, the HSI *classification* community has not systematically targeted training efficiency: most works still adopt standard training loops without explicitly staging learning to respect spectral structure and sensor heterogeneity. This gap motivates a curriculum that begins with information-preserving, low-cost spectra and progressively restores full spectral complexity as learning stabilizes.

We introduce *SpectralTrain*, a curriculum learning (CL) strategy tailored to the spectral dimension. Early phases replace the full spectrum with a principal component analysis (PCA)-compressed view that preserves dominant energy while suppressing noise; subsequent phases progressively increase the number of retained components until all bands are restored. This spectral curriculum stabilizes optimization, reduces Central Processing Unit (CPU)–Graphics Processing Unit (GPU) transfer and compute in initial epochs, and respects HSI band structure better than uniform or frequency-only truncation schemes. The procedure is agnostic to backbone, optimizer,

and loss, and applies to classical convolutional neural networks (CNNs), 3D spectral networks, and transformer-based models alike.

On Indian Pines, Salinas-A, and a climate-focused cloud classification dataset (CloudPatch-7), SpectralTrain yields $2\text{--}7\times$ faster training with comparable accuracy and robust behavior across different spatial scales and spectral characteristics. These results suggest that optimizing training schedules is a scalable lever for HSI, distinct from and compatible with architectural innovations and pretraining.

We summarize our contributions as follows:

- We articulate HSI-specific drivers of training inefficiency for classification—beyond generic high dimensionality—highlighting spectral structure, cross-sensor heterogeneity, and bandwidth-bound training.
- We propose SpectralTrain, a spectral curriculum using PCA-based band reduction in early phases and progressive restoration of full spectra, enabling low-to-high spectral–spatial learning at reduced cost.
- We demonstrate universality across backbones, optimizers, and losses on Indian Pines, Salinas-A, and CloudPatch-7, achieving $2\text{--}7\times$ speedups with minimal accuracy loss.
- We provide a simple, drop-in recipe that accelerates HSI classification training without modifying model architectures or loss functions.

2 Related Work

2.1 Training Strategy in Computer Vision

Recent advances in deep learning have highlighted the strength of pretraining frameworks that decouple representation learning from task-specific optimization. In natural language processing, models such as GPT [9] and BERT [10] pretrain on large corpora, while in computer vision, MAE [11] and DINO [12] learn transferable visual features, yielding notable gains in data efficiency and downstream performance [13]. However, these approaches typically require substantial compute and extensive data, which limits practicality for hyperspectral image (HSI) *classification*, where labels are scarce and the spectral axis dominates memory and I/O.

In parallel, task-specific training frameworks optimize schedules, inputs, and policies under domain or resource constraints [14, 15]. Examples include the self-supervised iterative framework (SITF) for 3D point cloud denoising [16] and Ddpg-AdaptConfig, a reinforcement learning policy for federated training under limited resources [17]. Among training-efficiency methods in computer vision, EfficientTrain++ [8] is a notable contribution: it adopts a resolution-based curriculum that gradually increases spatial input size to balance training cost and feature richness. Inspired by this spatial-domain idea, we ask how a curriculum should be designed for HSI classification. Unlike RGB images, HSI cubes exhibit contiguous, instrument-induced spectral structure and band-localized discriminative cues; applying resolution-only schedules does not exploit this spectral redundancy and may remove informative bands or cause unstable early gradients. This gap motivates a spectral-aware curriculum tailored specifically to HSI classification.

2.2 Curriculum Learning

Curriculum learning (CL) organizes the training process by presenting easier elements before harder ones [18]. Representative variants integrate fuzzy-clustered curricula for semi-supervised classification [19] and design multi-task curricula for weakly supervised learning [20]. Self-paced and difficulty-aware schedules further use optimization feedback or uncertainty estimation to select and weight samples, improving robustness to label noise and class imbalance [21]. These methods typically operate along sample-, label-, or objective-level difficulty and have proven effective for convergence and generalization.

Beyond sample ordering, curricula can also control the input signal itself (e.g., image resolution or augmentation strength) to shape the optimization landscape. However, most such designs assume RGB image statistics. In hyperspectral imaging, information is distributed along a contiguous spectral axis with instrument-specific responses, and class-discriminative cues are often band-localized rather than uniformly spread. Directly borrowing RGB-oriented curricula can therefore discard informative bands or destabilize early optimization.

We position SpectralTrain as a curriculum grounded in the spectral axis: training starts from an information-preserving principal component analysis (PCA) compression of spectra and progressively restores bands as learning stabilizes. This spectral curriculum preserves task-relevant components while reducing early-epoch compute and I/O. It is orthogonal to spatial or semantic curricula and is compatible with a wide range of architectures and loss functions.

2.3 Hyperspectral Imaging for Climate and Environment

Hyperspectral imaging has demonstrated considerable potential in climate and environmental monitoring [22]. By capturing per-pixel reflectance across contiguous wavelengths, it supports aerosol and gas detection, vegetation stress analysis, and water quality assessment through material-specific spectral signatures. These capabilities provide a fine-grained basis for environmental state estimation beyond broadband sensors.

Despite this potential, adoption in meteorology and climate prediction remains comparatively limited. We study cloud-type classification as a practical entry point: the CloudPatch-7 dataset [23] assembles hyperspectral cloud patches to analyze spectral and spatial patterns relevant to early-stage weather recognition. Spectral cues associated with particle size, phase (ice versus liquid water), and optical thickness complement spatial texture, offering a discriminative basis for automatic cloud typing.

Operational scenarios impose tight compute and memory budgets, while hyperspectral datacubes are large and bandwidth-bound. These constraints motivate efficient training frameworks that respect spectral structure. To the best of our knowledge, research on hyperspectral image classification largely continues to rely on conventional iterative training loops without staging learning along spectra; organizing training to begin with information-preserving spectral compression and to progressively restore full spectra is a natural design to manage early-epoch cost while retaining task-relevant signals.

3 Method

The SpectralTrain method represents a paradigm shift compared with previous approaches that focus on enhancing specific hyperspectral imaging models. Traditional hyperspectral research generally concentrates on optimizing a particular model's performance (e.g., fine-tuning feature extractors or classifiers). In contrast, SpectralTrain introduces a universal training framework that combines principal component analysis (PCA) based image-level spectral downsampling with a curriculum learning (CL) strategy, thereby redefining the training pipeline.

This framework is not confined to a single backbone; it is applicable to convolutional neural networks (CNNs), 3D spectral networks, and transformer-based models. PCA reduces input spectral dimension while preserving dominant information; CL organizes training from easy to hard by gradually restoring spectral complexity and increasing spatial resolution. A schematic overview is shown in Fig. 1.

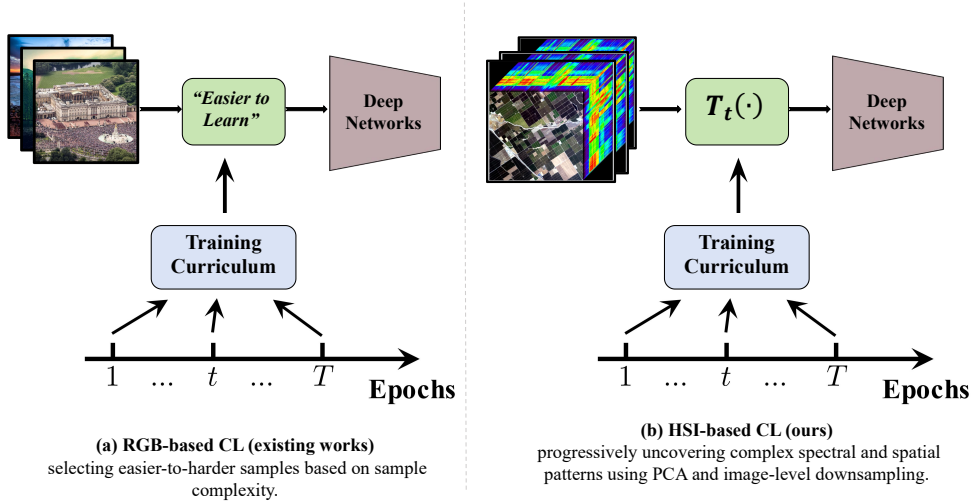


Fig. 1 Overview of SpectralTrain. (a) Discrete decision-making based on RGB sample difficulty (e.g., selecting easier low-frequency content first). (b) Hyperspectral imaging-based curriculum (ours): a continuous transformation $T_t(\cdot)$ progressively introduces complex spectral and spatial patterns via PCA-based spectral reduction and image-level downsampling, gradually increasing data complexity as training proceeds.

3.1 Computational Constraints and Optimization Objectives

We aim to maximize prediction accuracy under a fixed compute budget. Let total training epochs be $T = \beta T_0$, where T_0 is the baseline (full-cost) training epochs and $0 < \beta < 1$ is a pre-defined saving ratio. Training is divided into N curriculum stages.

Each stage uses a spatial resolution B_i and retains k_i principal components of the original spectral dimension D ($k_i \leq D$), with B_i and k_i increasing across stages.

A piecewise-continuous learning-rate scheduler $\alpha_{\text{lr}}(t_1:t_2)$ is adopted; the interval $((i-1)/N, i/N]$ is reserved for stage i . To balance compute across stages, we scale the number of optimization steps by spatial FLOPs:

$$\text{Steps}_i = \left\lfloor \frac{T}{N} \cdot \left(\frac{B_0}{B_i} \right)^2 \right\rfloor, \quad \text{since per-step FLOPs} \propto B^2 \text{ for standard convolutions.} \quad (1)$$

where B_0 is the original spatial size. For spectral compression, the transfer/computation reduction factor is

$$\text{Compression Ratio} = \frac{D}{k_i}, \quad (2)$$

which upper-bounds the saving in host-device transfer; activation memory also depends on architecture and depth when PCA is applied prior to upload.

3.2 Training Schedule and Stage Switching

SpectralTrain couples a spectral curriculum with a compute-balanced step allocation. At stage i , we (i) select or search a spatial resolution B_i (monotonic non-decreasing over stages) and (ii) monotonically increase k_i (e.g., linear, piecewise-linear, or validation-guided). PCA is computed on the CPU (per image or per scene) and applied before GPU upload; resizing to B_i is then performed.

We also allow a short proxy fine-tuning of T_{ft} epochs to select B_i from a candidate set \mathcal{B}_i under the fixed budget, extending the resolution-order search idea to hyperspectral training.

3.3 Constraint Factors and Training Process

Resolution-controlled steps.

Unlike fixed-size training, SpectralTrain adapts B_i per stage and balances compute using Eq. (1). Intuitively, smaller B_i yields more parameter updates early on (lower per-step cost), while larger B_i later preserves fine spatial structure when the model is ready to absorb it.

Spectral compression prior to upload.

Before transferring data to GPU, we apply PCA to compress the spectral axis to k_i components, reducing I/O and VRAM pressure with ratio D/k_i in Eq. (2). PCA can be computed per image or per scene on CPU and cached; the projection is applied on the fly to each mini-batch.

Stage switching.

Stages are synchronized with the scheduler α_{lr} over $((i-1)/N, i/N]$. At the boundary, we (optionally) perform a short fine-tuning of T_{ft} epochs at (B_i, k_i) to smooth the transition before moving to stage $i+1$.

Algorithm 1 SpectralTrain

3.4 Computational Constraint Order Search

We extend the resolution order-search idea to hyperspectral training by selecting B_i from \mathcal{B}_i with a short validation-guided proxy, while k_i follows a monotonic schedule (e.g., linear from k_1 to D). At stage i , we choose

$$\hat{B}_i = \arg \max_{B \in \mathcal{B}_i} \text{ValAcc}(\text{FineTune}(\Theta_{i-1}, \text{ReduceAndResize}(\mathcal{D}, k_i, B), T_{\text{ft}}, \alpha_{\text{lr}})), \quad (3)$$

then train for $Steps_i$ steps computed by Eq. (1). The above design decouples *what* the model sees (spectral/spatial complexity) from *how much* compute it receives

(steps), enabling progressive optimization under a fixed budget without modifying architectures or losses.

4 Results

4.1 Experimental Setup

The evaluation of SpectralTrain is conducted under controlled and comparable conditions. Three datasets spanning different spatial resolutions, band counts, and scene characteristics are considered: Indian Pines (145×145 , 200 bands), Salinas-A (86×83 , 204 bands), and CloudPatch-7 (50×50 , 462 bands). Training uses PyTorch 2.1.2, TorchVision 0.16.2, and TorchAudio 2.1.2 on CUDA 12.1/Python 3.10 with an Intel Core i7-13700 (16 threads), 32 GB RAM, and an NVIDIA RTX 4090D (24 GB); preprocessing and caching occur on a 50 GB NVMe SSD. Architectures include classical CNNs (ResNet-34 [24], ConvNeXt-T [25]), hybrid CNN-Transformer models (MetaFormer [26], ADGAN [27]), spectral-aware designs (3D-ConvSST [28], SQS [29]), and DSFormer [30]. Unless specified, data splits, optimizers, loss functions, and learning-rate schedules are shared. A conventional “full-spectrum from the first epoch” loop [31] serves as a reference when comparing with SpectralTrain. Metrics follow standard practice: Overall Accuracy (OA), Average Accuracy (AA), and Cohen’s Kappa.

Unless otherwise noted, all experiments on Indian Pines, Salinas-A, and CloudPatch-7 share the following training and regularization settings: batch size = 16, total epochs = 300 (warmup = 20 epochs, min LR = 1×10^{-6}), optimizer = AdamW (lr = 0.004, eps = 1×10^{-8} , weight decay = 0.05), label smoothing = 0.1, layer decay = 1.0, drop path = 0, head dropout = 0.0, layer-scale init = 1×10^{-6} , update_freq = 1, seed = 0.

Before analyzing curricula, it is useful to outline typical sensitivities of supervised pipelines. Under fixed data and augmentation, epoch count trades underfitting and overfitting: too few epochs lead to insufficient convergence, whereas excessive epochs increase variance and degrade generalization. Learning-rate schedules and optimizers shape the loss landscape explored during early training; distinct choices can lead to different convergence basins even with identical architectures. Loss definitions change margin properties and class imbalance handling. Batch size and gradient accumulation alter effective noise levels. Architectural depth and width affect capacity and inductive bias. In hyperspectral classification, these generic sensitivities are amplified by the contiguous spectral axis: compute and I/O scale with the number of bands, cross-sensor response functions induce domain shift, and discriminative cues are often band-localized and non-uniform. Consequently, training procedures that ignore spectral structure can incur unnecessary early-epoch cost and unstable optimization.

4.2 Ablative Study

Figure 2 summarizes the empirical motivation for a spectral curriculum. The two cluster-mean spectra from Indian Pines in panel A show that discriminative information concentrates in narrow, non-uniform wavelength intervals; removing bands

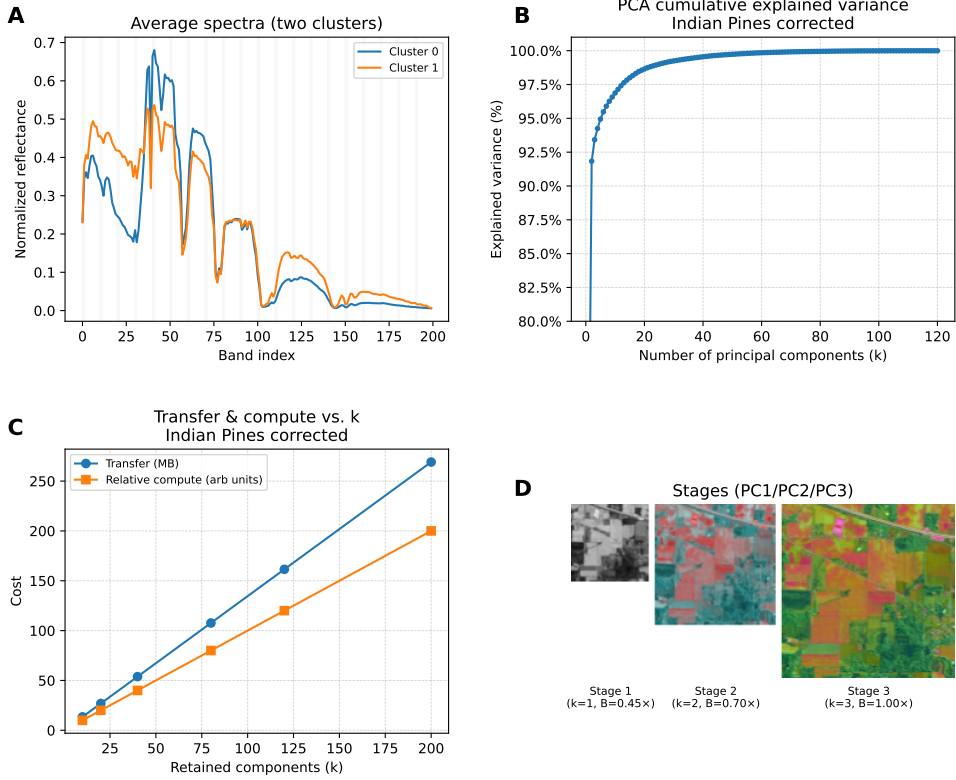


Fig. 2 Motivation example for a spectral curriculum on Indian Pines. (A) Average spectra of two clusters show band-localized discriminative cues, so uniform band dropping risks removing signals. (B) PCA cumulative explained variance illustrates that a small number of components preserve most energy, motivating an information-preserving low-cost start; PCA is used here as a representative linear compressor. (C) Per-epoch transfer and compute scale with the number of retained components k , so beginning with small k saves early cost. (D) Curriculum stages progressively increase both spectral components and spatial size (PC1/PC2/PC3 composites). Panels illustrate one instantiation with PCA; Table 3 shows that alternative reducers (UMAP/ICA) produce comparable behavior under the same staged schedule.

uniformly at the beginning can erase these cues at random. Panel B indicates that a small number of principal components captures most spectral energy on the same cube, which permits an information-preserving start. Panel C shows that host-to-device transfer and per-epoch compute grow approximately linearly with the number of retained components k , so using a small k early saves cost in the regime where gradients are still coarse. Panel D visualizes staged inputs that progressively restore spectral and spatial complexity. In combination, these diagnostics support the decision to organize training along spectra rather than fixing full cubes from the first epoch, which follows the spirit of resolution curricula in computer vision [8] while addressing hyperspectral specifics.

Table 1 Performance with different filters added. Time denotes seconds per epoch.

Settings	OA (%)	AA (%)	Kappa	Time (s/epoch)
Ours (PCA curriculum)	99.02	99.04	0.99	8.00
+ Savitzky–Golay	98.82	98.87	0.99	8.00
+ Gaussian	98.80	98.84	0.99	11.00
+ TV Denoising	98.87	98.91	0.99	8.00

All ablation experiments were conducted on the CloudPatch-7 Dataset. A first question is whether additional spectral filtering remains beneficial once information-preserving compression is applied. Table 1 keeps schedules fixed and appends Savitzky–Golay [32], Gaussian smoothing [33], or total-variation [34] denoising on top of PCA-based compression. The figures indicate no gains in OA/AA or Kappa and, for Gaussian smoothing, higher epoch time. After PCA concentrates low-rank structure, hand-crafted smoothing becomes redundant while adding cost.

The schedule itself is then compared against a conventional loop [31] across heterogeneous backbones while holding splits, optimizer, loss, and learning-rate schedule constant. Table 2 shows that SpectralTrain reduces seconds per epoch by about 2–7 \times with comparable accuracy. For 3D-ConvSST, time drops from 28s to 4s while Kappa remains 0.99; for RCNN, time decreases from 38s to 6s with OA/AA near 99.44%/99.42%. This points to early-epoch staging along the spectral axis as an effective lever for efficiency that does not rely on architecture-specific tuning.

Sensitivity to the compression operator was evaluated by replacing PCA with UMAP or ICA while keeping the curriculum stage boundaries, the learning-rate schedule, and the per-stage compute budgets fixed. As shown in Table 3, all three reducers achieve comparable OA/AA at the same time per epoch, indicating that the staged restoration of spectral complexity—rather than the particular manifold mapping—drives the efficiency gains. When the retained dimensionality k is very small, non-linear reducers can yield slightly larger validation margins for some classes; as k increases and the full spectrum is restored, these differences quickly diminish, consistent with using the reducer only for a low-cost warm-up. Overall, SpectralTrain does not rely on the linearity of PCA and remains effective with any information-preserving compressor that is approximately nested across k (i.e., the representation at k is largely contained in that at $k' > k$).

Loss definitions are compared next [35–37]. Table 4 indicates that cross entropy, multi-label soft margin, and binary cross entropy with logits yield similar OA/AA and Kappa at the same epoch time. In standard practice, distinct losses can change margin behavior, calibration, and robustness, thereby altering performance; under the staged spectral schedule, these differences are attenuated, consistent with a smoother early optimization landscape.

Optimizer choice is evaluated in Table 5. In conventional settings, AdamW [38], AdamMini [39], and SGD [40] often exhibit different convergence speed and final

Table 2 Comparison of conventional training and SpectralTrain using PCA downsampling. All models share the same splits and hyperparameters within each column group. Times measured on the same hardware; seeds fixed unless stated.

Model	Current SOTA Training [31]				SpectralTrain		
	Time (s/epoch)	OA (%)	AA (%)	Kappa	Time (s/epoch)	OA (%)	AA (%)
ResNet-34	113	98.55	98.59	0.98	66	98.20	98.05
ADGAN	664	98.96	98.91	0.98	298	98.28	98.10
MetaFormer	77	98.93	98.98	0.99	17	98.95	98.94
ConvNeXt-T	269	99.06	99.14	0.99	94	99.15	99.18
SQS	356	99.30	99.30	0.99	254	98.17	98.11
3D-ConVSST	28	99.84	99.76	0.99	4	99.02	99.04
RCNN	38	99.75	99.76	0.99	6	99.44	99.42

Table 3 Performance with different dimensionality reduction methods.

Dimensionality Reduction Method	OA (%)	AA (%)	Kappa	Time (s/epoch)
PCA	99.15	99.18	0.99	8.00
UMAP	99.36	99.39	0.99	8.00
ICA	98.89	98.86	0.99	8.00

Table 4 Performance and efficiency of different loss functions.

Loss Function	OA (%)	AA (%)	Kappa	Time (s/epoch)
Cross Entropy Loss	98.96	99.01	0.99	8.00
Multi-Label Soft Margin Loss	98.96	98.97	0.99	8.00
Binary Cross Entropy with Logits	99.02	99.04	0.99	8.00

Table 5 Performance with different optimizers.

Optimizer	OA (%)	AA (%)	Kappa	Time (s/epoch)
AdamW	99.15	99.18	0.99	8.00
AdamMini	98.95	98.99	0.99	8.00
SGD	98.82	98.83	0.99	8.00

accuracy because of distinct momentum and regularization properties. Under the spectral curriculum, all three converge effectively with small spread, indicating reduced sensitivity once early spectral complexity is aligned with learning progress.

Epoch count is varied between 50 and 600 in Table 6 with stage budgets scaled proportionally. In common pipelines, too few epochs lead to underfitting and too many risk overfitting; the observed plateau with a peak near 300 epochs indicates that staged spectra guide optimization toward a stable basin without intensive schedule tuning.

4.3 Cross-dataset Study

Cross-dataset behavior and the relation to recent architectures are summarized in Tables 7–9. On Indian Pines, several backbones paired with SpectralTrain reach OA around or above 98.7%, whereas DSFormer trained with its default settings performs worse on this dataset. On Salinas-A, accuracy remains high despite larger spectral variability. On CloudPatch-7 with 462 bands, most models approach 99% OA/AA with Kappa at or above 0.98. Instances where an earlier architecture with SpectralTrain exceeds DSFormer are better interpreted not as an absolute statement about model capacity but as evidence that modern designs may be over-optimized for full-spectrum-from-epoch-1 regimes; reshaping early optimization through an information-preserving

Table 6 Performance comparison across different epochs.

Epoch	OA (%)	AA (%)	Kappa
50	98.67	98.67	0.99
100	98.80	98.88	0.99
200	98.87	98.93	0.99
300	99.15	99.18	0.99
400	98.98	98.98	0.99
500	98.86	98.94	0.99
600	99.00	99.00	0.99

Table 7 Performance comparison on Indian Pines dataset.

Model	OA (%)	AA (%)	Kappa
ADGAN	97.37	94.59	0.97
MetaFormer	94.34	93.31	0.94
ConvNeXt-T	98.72	99.12	0.99
SQS	94.02	97.30	0.94
3D-ConvSST	90.95	84.56	0.91
RCNN	98.33	98.71	0.98
DSFormer	90.58	77.05	0.91

Table 8 Performance comparison on Salinas-A dataset.

Model	OA (%)	AA (%)	Kappa
ADGAN	92.69	94.23	0.93
MetaFormer	94.10	94.22	0.94
ConvNeXt-T	98.09	97.86	0.98
SQS	95.02	95.37	0.95
3D-ConvSST	97.35	96.65	0.97
RCNN	98.09	98.02	0.98
DSFormer	91.20	89.81	0.91

spectral schedule reduces reliance on capacity alone. This interpretation supports the joint design of architectures and training schedules in hyperspectral learning.

The backbone-level trends are summarized in Figures 3 and 4. Figure 3 reports overall accuracy (OA) and average accuracy (AA) for different ResNet and ConvNeXt variants; Figure 4 reports Cohen’s Kappa for the same variants. In conventional hyperspectral image classification, model depth and width often exert a pronounced effect on performance because larger capacity and receptive fields typically improve feature expressiveness. Under the proposed spectral curriculum, the dispersion across depth scales is small: OA and AA remain consistent from shallow to deep variants (for

Table 9 Performance comparison on CloudPatch-7 dataset.

Model	OA (%)	AA (%)	Kappa
ADGAN	98.28	98.10	0.98
MetaFormer	98.95	98.94	0.99
ConvNeXt-T	99.15	99.18	0.99
SQS	98.17	98.11	0.98
3D-ConvSST	99.02	99.04	0.99
RCNN	99.44	99.42	0.99
DSFormer	93.75	93.81	0.94

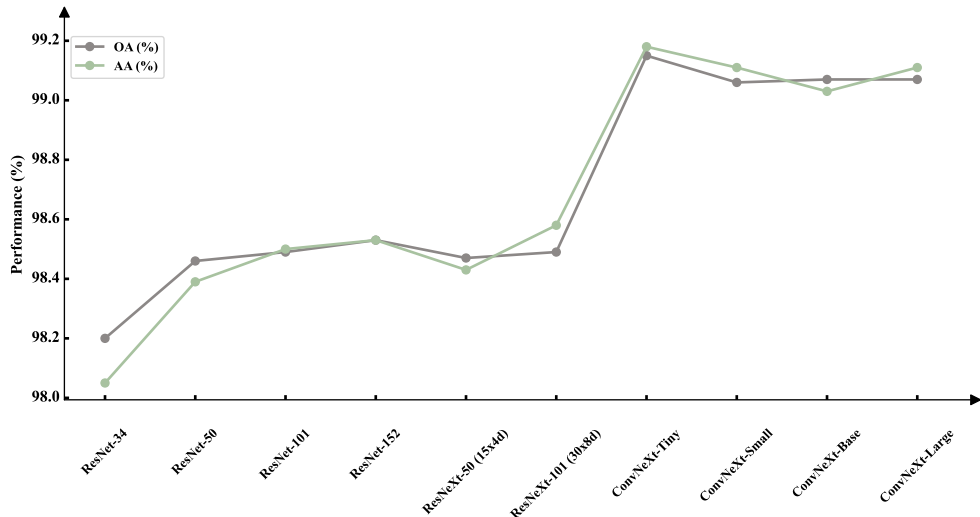


Fig. 3 OA/AA across backbone scales under SpectralTrain.

example, ResNet-34 to ResNet-152 and ConvNeXt-Tiny to ConvNeXt-Large), and Kappa values cluster around 0.99. These observations indicate that aligning the training schedule with spectral structure reduces the usual sensitivity to backbone depth and receptive-field configuration, which is consistent with the hypothesis that early spectral staging mitigates over-dependence on capacity.

4.4 Hyperspectral Cloud Scene Understanding

Inspired by the human practice of "reading clouds to predict weather," this study introduces the CloudPatch-7 dataset as the first dedicated hyperspectral benchmark for cloud-type classification under extreme weather conditions. This novel approach bridges atmospheric remote sensing and hyperspectral representation learning, enabling a fine-grained understanding of cloud morphology and its relationship to

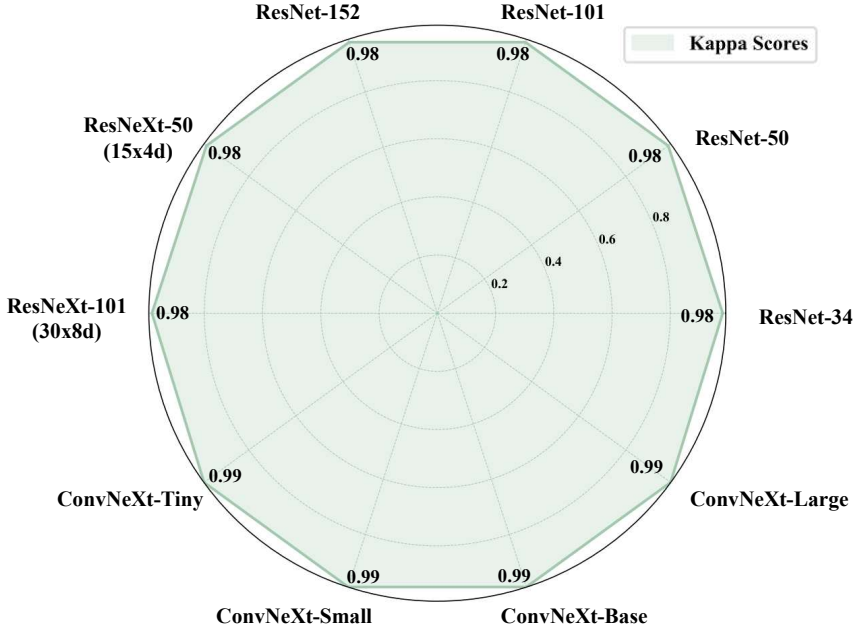


Fig. 4 Kappa across ResNet and ConvNeXt variants under SpectralTrain.

severe weather patterns by leveraging the rich spectral-spatial information captured by hyperspectral sensors.

The CloudPatch-7 dataset consists of 380 curated HSI patches (50×50 pixels) extracted from 28 full-scene captures, spanning a continuous spectral range of 462 bands from 400 to 1000 nm. The patches are classified into seven meteorological categories: dense dark cumuliform clouds, dense bright cumuliform clouds, semi-transparent cumuliform clouds, dense cirroform clouds, semi-transparent cirroform clouds, clear sky with low aerosol scattering, and clear sky with moderate to high aerosol scattering. These labels represent key atmospheric features relevant to climate monitoring and extreme weather forecasting. To assess the effectiveness of SpectralTrain in atmospheric scene understanding, we performed classification experiments on CloudPatch-7 using seven representative model architectures across three structural paradigms: classical CNNs (ResNet-34, ConvNeXt-T), hybrid convolutional-transformer models (MetaFormer, ADGAN), and spectral-aware models designed for HSI processing (3D-ConvSST, SQS, DSFormer). Despite significant architectural differences, SpectralTrain consistently enabled all models to achieve high classification accuracy. Notably, even under limited computational resources and without pretraining, SpectralTrain preserved fine-grained spectral distinctions, enabling the separation of subtle atmospheric classes, such as semi-transparent cirroform clouds and high-scattering clear skies.

The robustness of these results underscores the practical applicability of SpectralTrain for cloud-type classification tasks in environmental monitoring. Accurate recognition of dense cumuliform or cirroform structures, for example, facilitates more precise tracking of convective storms and jet stream activity—key indicators of extreme weather events. Additionally, the ability to differentiate aerosol scattering levels from clear-sky signatures presents opportunities for high-resolution air quality monitoring.

Beyond the current scope, the consistently high performance observed across diverse models suggests that SpectralTrain may serve as a foundation for large-scale cloud analytics pipelines. Future work may explore integrating this framework with satellite-based imaging modalities and spatiotemporal modeling techniques to support long-term climate observation and early warning systems. Moreover, extending the CloudPatch series to include multi-temporal cloud dynamics or joint spectral–thermal modalities could further broaden the impact of hyperspectral learning in meteorological research.

5 Discussion

This study reframes hyperspectral image classification as a setting where training efficiency must be considered alongside architectural design. The motivation figure (Figure 2) highlights properties unique to hyperspectral data—band-localized cues, contiguous instrument responses, and bandwidth-bound pipelines—that render RGB-oriented efficiency recipes ill-suited. SpectralTrain organizes optimization along the spectral axis: training begins with an information-preserving compression and progressively restores full spectra as learning stabilizes. To the best of our knowledge, this is the first training-efficiency strategy targeted specifically at hyperspectral classification.

EfficientTrain++ [8] showed that a resolution-based curriculum can reduce early-epoch cost for RGB recognition. SpectralTrain is inspired by this idea but departs in a fundamental way: the schedule acts on spectral complexity rather than spatial resolution. The distinction matters because spectral aliasing, cross-sensor response shifts, and early-epoch bandwidth limits are organized along wavelength, not space. The two directions are complementary, and a joint spatial–spectral curriculum is a natural extension.

Under the proposed schedule, several mid-capacity or earlier backbones match or surpass DSFormer [30] on multiple datasets, whereas conventional training [31] tends to favor the modern architecture. This pattern suggests that recent state-of-the-art systems may be over-optimized for the standard training paradigm. Aligning the schedule with spectral structure attenuates sensitivity to depth, receptive field, and token mixers, indicating that peak accuracy and efficiency in hyperspectral classification are best pursued through co-design of architectures and training strategies. Reporting both a conventional and a curriculum-aligned protocol, as in Table 2, provides a fairer basis for architectural comparison.

The framework’s scope is bounded by several practical considerations. First, if rare classes concentrate in late spectral components, early compression can delay their separation; class-aware staging or mixing a small fraction of full-spectrum samples into the warm-up mitigates this effect. Second, when spectra are short or the pipeline

is compute- rather than I/O-bound, the wall-clock gain narrows even though the method remains valid. Third, strong cross-sensor response mismatch may require re-estimating stage boundaries or per-sensor compression bases to preserve early-phase stability. Importantly, the method does not rely on the linearity of PCA: replacing PCA with UMAP or ICA while keeping the curriculum boundaries, learning-rate schedule, and budgets unchanged yields comparable OA/AA (Table 3), indicating that staged restoration of spectral complexity—rather than a specific manifold mapping—is the principal driver of efficiency.

Two forward directions follow. For dense prediction, the same spectral curriculum can be applied at the patch or pixel level with segmentation encoders and decoders; this track is orthogonal to segmentation pretraining [41, 42] and tests whether curriculum-aligned optimization improves boundary fidelity without added inference cost. For climate applications, multimodal cloud analysis that fuses hyperspectral, thermal, and active sensors (e.g., radar or LiDAR) would benefit from a modality-aware curriculum in which early phases operate on a low-cost spectral subspace with down-weighted auxiliary streams, followed by progressive increases in spectral rank and modality weights. Such schedules preserve the system-level advantages (lower transfers, smaller activations, larger feasible batches) underlying the observed 2–7× acceleration.

6 Conclusion

SpectralTrain is a training schedule for hyperspectral classification that starts from an information-preserving compressed spectrum and progressively restores full spectral complexity. Across Indian Pines, Salinas-A, and CloudPatch-7, the approach reduces training time by 2–7× at comparable accuracy under diverse backbones, optimizers, losses, and epoch budgets. The findings indicate that efficiency in hyperspectral learning is governed as much by the schedule as by the architecture; co-designing the two yields more reliable speed–accuracy trade-offs than optimizing either in isolation. Future work will extend the curriculum to dense prediction with segmentation backbones and to multimodal cloud analysis in which hyperspectral data are fused with thermal and active sensors, aiming to retain the same resource profile while improving scene-level understanding.

Conflict of interest

The authors declare that they have no conflicts of interest or competing interests.

Compliance with ethical standards

This study did not involve human participants or animals. It relies solely on publicly available benchmark datasets and open-source code; therefore, approval from an institutional review board or ethics committee was not required. All authors have read and approved the final manuscript and agree with its submission.

Informed consent

Not applicable. The study uses only publicly available, de-identified datasets; any consent was obtained by the original data providers in accordance with their policies.

Data availability

The experimental data and the codes that support the findings of this study are available in Github with the identifier <https://github.com/mh-zhou/SpectralTrain>.

Appendix A CloudPatch-7: Dataset Summary and Supplementary Visualizations

CloudPatch-7 is a hyperspectral benchmark for cloud-type classification under extreme-weather-relevant conditions. It comprises 380 manually annotated image patches of size 50×50 pixels extracted from 28 larger parent scenes (approximately 5000×1500 pixels each). Seven atmospheric categories are defined: dense dark cumuliform (46), dense bright cumuliform (77), semi-transparent cumuliform (72), dense cirroform (25), semi-transparent cirroform (28), clear sky with low aerosol scattering (68), and clear sky with moderate-to-high aerosol scattering (64). Across all patches there are $380 \times 50 \times 50 = 950,000$ labeled pixels, each with 462 spectral bands within 400–1000 nm. The figures below summarize class balance and spectral statistics from code-generated analyses.

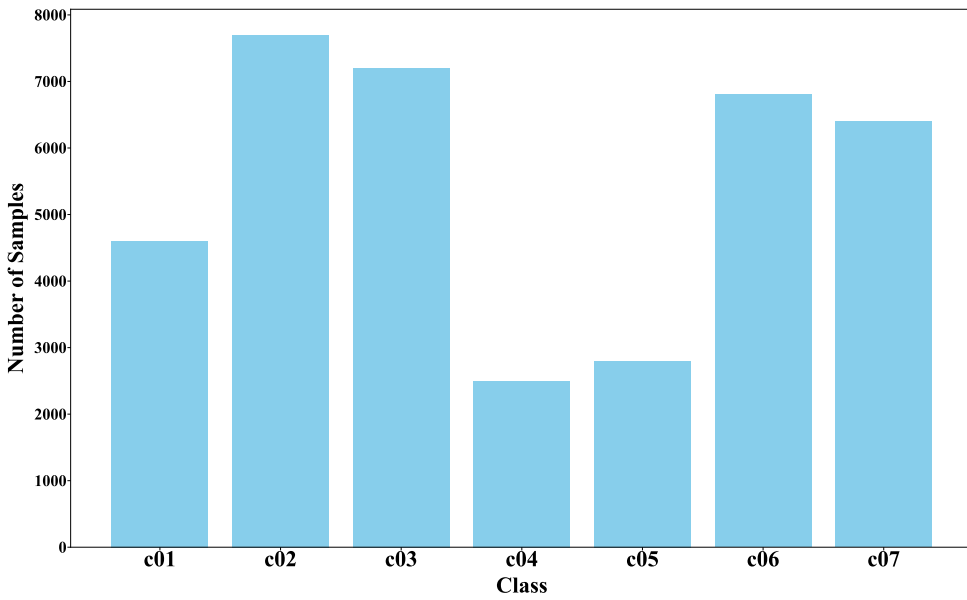


Fig. A1 Supplementary Figure S1. Class distribution in CloudPatch-7. Bars show per-class sample counts (c01–c07), revealing moderate imbalance.

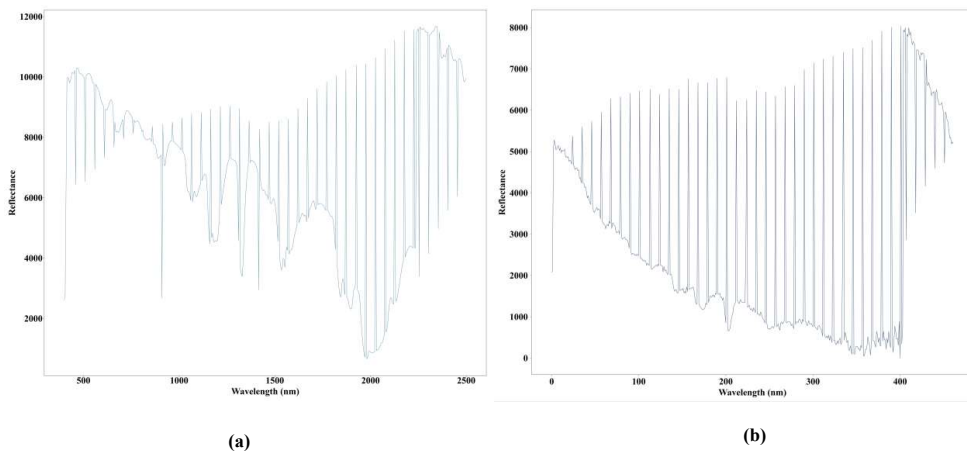


Fig. A2 Supplementary Figure S2. Spectral reflectance curves. Left (a): class-wise mean spectra; Right (b): a representative single-pixel spectrum. Axes are reflectance (vertical) and wavelength index (horizontal).

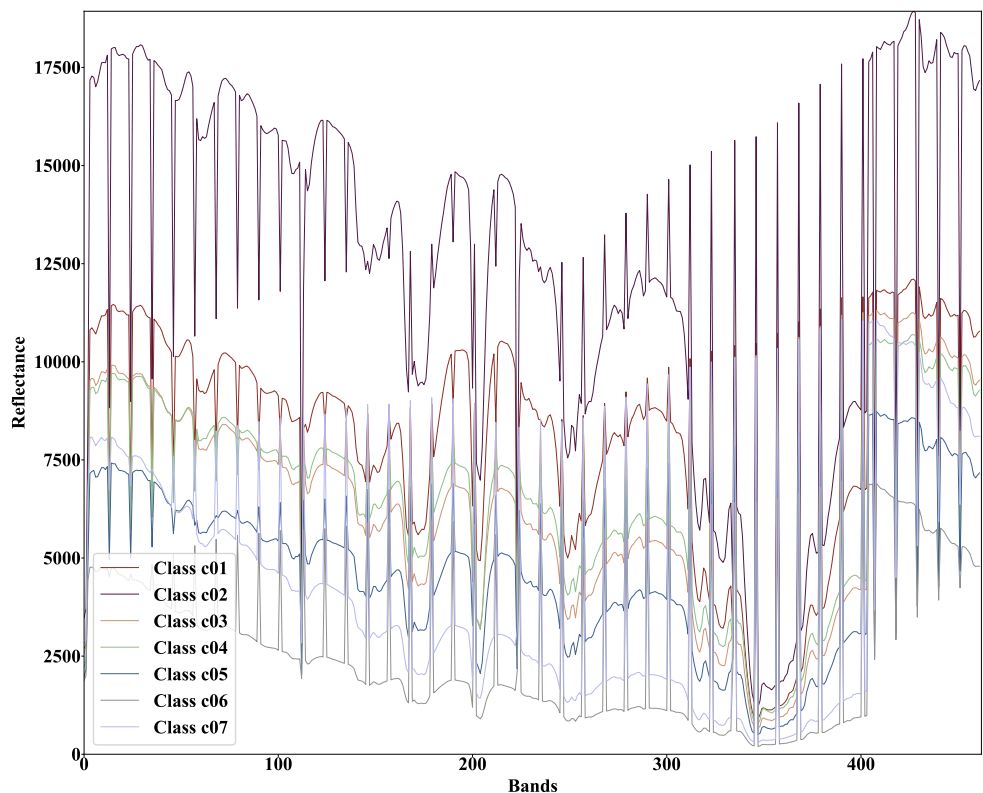


Fig. A3 Supplementary Figure S3. Average reflectance spectra for the seven classes (c01–c07). Distinct spectral shapes and band-localized differences provide discriminative cues.

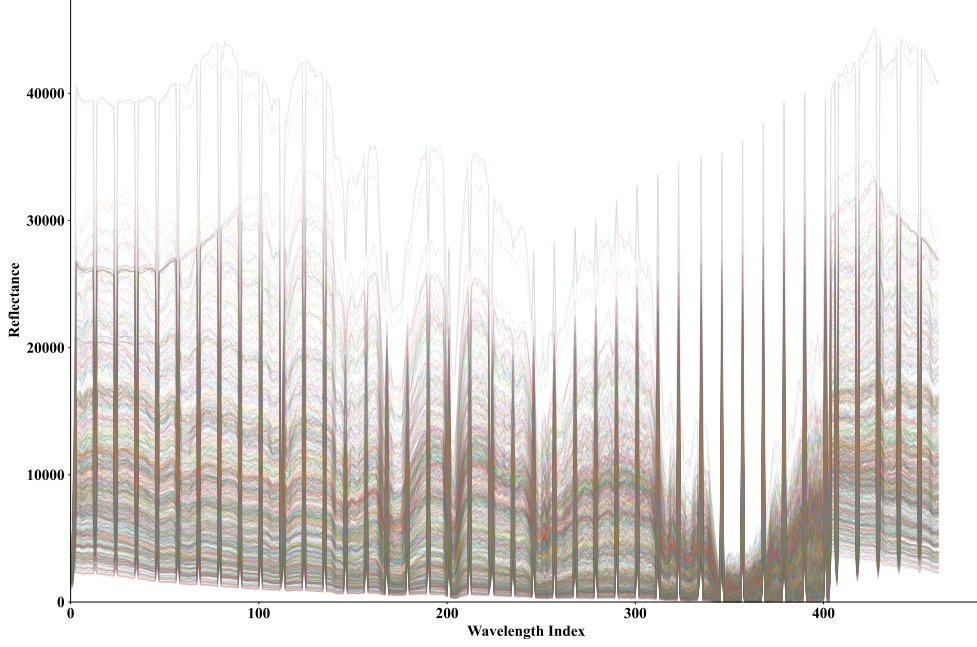


Fig. A4 Supplementary Figure S4. Dense overlay of per-sample spectra. Overlaid curves emphasize intra-class variability and contiguous, instrument-governed spectral ordering.

Appendix B Supplement B: Mathematical justification for PCA-first sampling versus low-frequency cropping

Setting and notation.

A hyperspectral image (HSI) is a function $I : \Omega \times \Lambda \rightarrow \mathbb{R}$ with spatial domain $\Omega \subset \mathbb{R}^2$ and $\Lambda = \{\lambda_1, \dots, \lambda_N\}$. For a pixel $p = (x, y) \in \Omega$, the spectrum is $s(p) = [I(p, \lambda_1), \dots, I(p, \lambda_N)]^\top \in \mathbb{R}^N$. Stacking M pixels row-wise yields $X \in \mathbb{R}^{M \times N}$. The 2D spatial Fourier transform is denoted $\hat{f} = \mathcal{F}\{f\}$; the convolution theorem and Parseval identity follow standard references [43, 44]. PCA is defined on the centered matrix $\tilde{X} = X - \mathbf{1}_M \mu^\top$ with $\mu = \frac{1}{M} \sum_{i=1}^M X_{i,:}$; the spectral covariance is $C = \frac{1}{M-1} \tilde{X}^\top \tilde{X} = E \Lambda E^\top$ with $\lambda_1 \geq \dots \geq \lambda_N \geq 0$ [45].

B.1 Low-frequency cropping (LFC): spatial blurring, spectral distortion, and irreversibility

Ideal low-pass cropping.

For each band λ_j ,

$$\widehat{I}'(u, v, \lambda_j) = \widehat{I}(u, v, \lambda_j) H(u, v), \quad H(u, v) = \mathbf{1}\{\sqrt{u^2 + v^2} \leq f_c\}.$$

By the convolution theorem, $I'(\cdot, \cdot, \lambda_j) = I(\cdot, \cdot, \lambda_j) * h$ with $h = \mathcal{F}^{-1}\{H\}$ (for the circular ideal low-pass, $h(r) = \frac{2f_c J_1(2\pi f_c r)}{r}$, $r = \sqrt{x^2 + y^2}$).

Proposition 1 (Contraction under LFC) *Let $\mathcal{T}_H : f \mapsto f * h$. Since $|H| \leq 1$, $\|\mathcal{T}_H f\|_{L^2} \leq \|f\|_{L^2}$ and $\|\mathcal{T}_H f - \mathcal{T}_H g\|_{L^2} \leq \|f - g\|_{L^2}$. Thus pairwise separations in L^2 contract band-wise under LFC.*

Proof. $\|\mathcal{F}\{f * h\}\|_2 = \|\widehat{f} H\|_2 \leq \|\widehat{f}\|_2$ and Parseval [43, 44]. \square

Per-pixel spectral mixing.

At pixel p ,

$$s'(p) = \int_{\Omega} s(q) h(p - q) dq.$$

If $h \geq 0$ and $\int h = 1$ (typical of Gaussian or other practical low-pass filters), $s'(p)$ is a convex average of neighboring spectra. In mixed-class neighborhoods this shrinks between-class contrasts.

Proposition 2 (Irrecoverable high-frequency energy loss) *For band λ_j ,*

$$E_{\text{lost}}(\lambda_j) = \int_{\sqrt{u^2 + v^2} > f_c} |\widehat{I}(u, v, \lambda_j)|^2 du dv > 0$$

unless the band is already band-limited below f_c . Hence I is not recoverable from I' in general.

Proof. Pointwise truncation in the Fourier domain and Parseval [44]. \square

B.2 PCA-first projection: optimal variance preservation without spatial averaging

Let $E_K = [e_1, \dots, e_K] \in \mathbb{R}^{N \times K}$ and $P_K = E_K E_K^\top$. PCA features are $Y = \tilde{X} E_K \in \mathbb{R}^{M \times K}$.

Theorem 3 (Eckart–Young–Mirsky) *Among all rank- K linear reconstructions, PCA uniquely minimizes*

$$\min_{\text{rank}(B) \leq K} \|X - (\mathbf{1}_M \mu^\top + Z B^\top)\|_F^2 = \|\tilde{X} - \tilde{X} P_K\|_F^2 = \sum_{i=K+1}^N \lambda_i.$$

PCA acts pointwise in space: $z(p) = E_K^\top \tilde{s}(p)$, hence it does not perform any cross-pixel averaging and preserves spectral purity up to an orthogonal projection [45].

B.3 Image-level sampling after PCA: aliasing control without spectral distortion

Let $y_k(x, y) = e_k^\top \tilde{s}(x, y)$ be the k -th principal component (PC) image. After prefiltering with a normalized low-pass g , sample by an integer factor $d \geq 2$:

$$y_k^{\downarrow d}[m, n] = (y_k * g)(md, nd), \quad m, n \in \mathbb{Z}.$$

Proposition 4 (Nyquist-consistent sampling per PC) *If the passband of g contains all spatial frequencies of y_k below π/d in each axis, sampling introduces no aliasing [43, 46]. The reconstructed spectrum at (md, nd) equals $\tilde{s}(md, nd) = \mu + E_K y_k^{\downarrow d}(md, nd)$, which lies in the PCA subspace and is free of cross-band spectral mixing; spatial averaging still occurs but is controlled by a Nyquist-consistent anti-aliasing filter.*

For class means m_a, m_b and a positive-definite pooled covariance Σ , the subspace Mahalanobis distance

$$\mathcal{D}_K^2 = (m_a - m_b)^\top P_K \Sigma^{-1} P_K (m_a - m_b)$$

matches the full-space value when between-class displacement concentrates in leading eigendirections, consistent with negligible accuracy loss once K passes the energy knee.

B.4 Direct comparison and systems implications

Proposition 5 (Separation versus approximation) *In mixed-class neighborhoods, LFC yields $s'(p) = \int s(q) h(p - q) dq$ and strictly reduces between-class separations whenever h has nontrivial spatial support. PCA-first plus Nyquist-consistent sampling changes spectra only by orthogonal projection P_K (non-expansive) and preserves separations within the retained subspace.*

Sketch. Proposition 1 and orthogonality of P_K [45]. □

Complexity.

For an $H \times W \times N$ cube and batch size B , host-to-device transfer is $\Theta(HWNB)$. After PCA to K bands and spatial downsampling by d per axis, the volume becomes $\frac{K}{N} \frac{1}{d^2} HWNB$, proportionally reducing transfer time and activation footprint. Empirical speedups align with bandwidth-bound training regimes.

Summary.

LFC realizes a band-wise spatial convolution that contracts discriminative separations and irreversibly discards high-frequency energy, distorting per-pixel spectra

central to HSI classification [47, 48]. PCA-first preserves dominant spectral variance with an explicit error budget (Theorem 3), avoids spatial averaging, and—when followed by Nyquist-consistent image-level sampling—reduces cost without aliasing-induced spectral distortion [43, 45, 46]. These facts justify the curriculum design that begins with information-preserving spectral compression and progressively restores full spectra as learning stabilizes.

Appendix C Supplement C: Detailed Step-by-Step Analysis of SpectralTrain

This supplement gives a rigorous derivation showing why SPECTRALTRAIN achieves faster time-to-accuracy without degrading accuracy. The argument proceeds in tightly linked steps: (i) *cost model* \rightarrow (ii) *PCA optimality* \rightarrow (iii) *conditioning and stochastic noise reduction* \rightarrow (iv) *curriculum time-to- ε bounds* \rightarrow (v) *numerical instantiation*.

C.1 Data, Notation, and Per-Step Cost

Standing assumptions.

Let $X \in \mathbb{R}^{M \times N}$ be the hyperspectral training matrix obtained by flattening $H \times W$ spatial locations ($M = HW$) and stacking per-pixel spectra $s_i \in \mathbb{R}^N$ as rows. The centered data are $\tilde{X} = X - \mathbf{1}_M \mu^\top$ with $\mu = \frac{1}{M} \sum_{i=1}^M s_i$. The spectral covariance is

$$C = \frac{1}{M-1} \tilde{X}^\top \tilde{X} = E \Lambda E^\top, \quad \Lambda = \text{diag}(\lambda_1, \dots, \lambda_N), \quad \lambda_1 \geq \dots \geq \lambda_N \geq 0.$$

Definition C.1 (Baseline per-step cost).

For a mini-batch of B pixels, the CPU–GPU transfer and first-layer FLOPs scale linearly with N :

$$T_{\text{step}}(N) = c_0 + c_1 N, \quad (\text{C1})$$

where c_0 collects N -independent costs (e.g., kernel launch, fixed compute) and c_1 captures N -linear I/O/compute. After PCA compression to $K \ll N$ bands,

$$T_{\text{step}}(K) = c_0 + c_1 K \ll T_{\text{step}}(N). \quad (\text{C2})$$

C.2 Why naive low-frequency cropping is suboptimal

Consider ideal circular low-pass filtering of each band image $I(\cdot, \cdot, \lambda_j)$ in the 2D spatial Fourier domain. Let \hat{I} be its Fourier transform and H the indicator of the radius- f_c disk. Then

$$\hat{I}'(u, v, \lambda_j) = \hat{I}(u, v, \lambda_j) H(u, v) \iff I'(\cdot, \cdot, \lambda_j) = I(\cdot, \cdot, \lambda_j) * h,$$

where $h = \mathcal{F}^{-1}\{H\}$ and $*$ denotes convolution (Parseval and convolution theorems; see, e.g., [44]).

Lemma C.2 (Spatial mixing contracts separations).

Suppose $h \geq 0$ and $\int h = 1$. For any pixel p ,

$$s'(p) = \int_{\Omega} s(q) h(p - q) dq$$

is a convex-like average of neighboring spectra, so for any two class means m_a, m_b , $\|m'_a - m'_b\|_2 \leq \|m_a - m_b\|_2$, with strict inequality when classes overlap within $\text{supp}(h)$.

Lemma C.3 (Irreversible high-frequency loss).

The removed energy per band equals

$$E_{\text{lost}}(\lambda_j) = \int_{\sqrt{u^2+v^2} > f_c} |\widehat{I}(u, v, \lambda_j)|^2 du dv > 0$$

for any non band-limited image; thus I' is generally non-invertible (Parseval [44]).

Together, Lemmas C.2–C.3 show low-frequency cropping (LFC) injects label-agnostic spatial averaging and permanently discards information, both undesirable for per-pixel HSI classification.

C.3 PCA compression preserves information optimally without mixing

Proposition C.4 (Eckart–Young–Mirsky).

For any $K \leq N$,

$$\min_{B \in \mathbb{R}^{N \times K}} \|\tilde{X} - \tilde{X}BB^\top\|_F^2 = \|\tilde{X} - \tilde{X}E_K E_K^\top\|_F^2 = \sum_{i=K+1}^N \lambda_i,$$

where $E_K = [e_1, \dots, e_K]$ are the top- K eigenvectors of C [45]. The per-pixel map $\tilde{s} \mapsto z = E_K^\top \tilde{s}$ is spatially *pointwise* (no cross-pixel mixing).

Variance retention.

Choosing K with $\sum_{i=1}^K \lambda_i / \sum_{i=1}^N \lambda_i \geq \eta$ (e.g., $\eta = 0.95$) retains at least an η fraction of spectral variance with an explicit tail error budget $\sum_{i>K} \lambda_i$.

C.4 Nyquist-consistent downsampling of principal components

Let $y_k(x, y) = e_k^\top \tilde{s}(x, y)$ denote the k -th PC image. Prefilter each y_k with a low-pass g that removes spatial frequencies above π/d in both axes, then subsample by an integer factor $d \geq 2$:

$$y_k^{\downarrow d}[m, n] = (y_k * g)(md, nd).$$

By the Shannon–Nyquist criterion, properly chosen g prevents aliasing and permits reconstruction from $y_k^{\downarrow d}$ [43, 46]. The reconstructed spectral vector at (md, nd) satisfies

$$\hat{s}(md, nd) = \mu + E_K y^{\downarrow d}(md, nd) \in \text{span}(E_K),$$

preserving spectral purity. Unlike LFC, this per-PC procedure introduces no cross-pixel spectral mixing.

C.5 Complexity reduction

Lemma C.5 (Cost reduction factor).

With PCA to K bands and spatial downsampling by d , the per-step data volume/FLOPs scale by

$$\frac{T_{\text{step}}^{(\text{PCA+DS})}}{T_{\text{step}}^{(\text{full})}} = \frac{K}{N} \cdot \frac{1}{d^2}. \quad (\text{C3})$$

Proof. The batch contains B pixels. After compression, each pixel has K features and the spatial grid shrinks to $(H/d) \times (W/d)$, giving $(HW/d^2) \cdot K \cdot B$ elements vs. $HW \cdot N \cdot B$ originally. \square

Example C.6.

For $N = 200$, $K = 20$ and $d = 2$, the first-stage per-step cost is $(20/200) \cdot (1/4) = 2.5\%$ of full cost.

C.6 Conditioning and stochastic noise: why convergence improves

We analyze a regularized empirical risk with a convex loss ℓ :

$$\mathcal{L}_N(w) = \frac{1}{M} \sum_{i=1}^M \ell(\langle w, s_i \rangle, y_i) + \frac{\lambda}{2} \|w\|_2^2, \quad \lambda > 0. \quad (\text{C4})$$

Let $\phi(t, y) = \partial \ell(t, y) / \partial t$ and assume $|\phi(t, y) - \phi(t', y)| \leq L_\phi |t - t'|$ (e.g., logistic has $L_\phi \leq 1/4$).

Lemma C.7 (Smoothness and strong convexity).

The gradient of \mathcal{L}_N is L_N -Lipschitz with

$$L_N \leq L_\phi \lambda_1 + \lambda,$$

and \mathcal{L}_N is μ_N -strongly convex with $\mu_N \geq \lambda$. For squared loss, $\mu_N = \lambda_N + \lambda$.

Corollary C.8 (Condition number improves under PCA).

In the PCA- K subproblem, the covariance becomes $C_K = E_K^\top C E_K = \text{diag}(\lambda_1, \dots, \lambda_K)$, so

$$\kappa_K = \frac{L_K}{\mu_K} \leq \frac{L_\phi \lambda_1 + \lambda}{\lambda_K + \lambda} \ll \kappa_N = \frac{L_\phi \lambda_1 + \lambda}{\lambda_N + \lambda},$$

because $\lambda_K \gg \lambda_N$ when the spectrum decays.

Lemma C.9 (SGD variance reduction).

Let $g(w; \xi)$ be an unbiased single-sample gradient. If $|\phi(t, y)| \leq C_\phi$ and $\mathbb{E}\|s\|_2^2 < \infty$, then

$$\text{Var}[g(w; \xi)] \preceq C_\phi^2 C.$$

After PCA to K , the variance trace bound drops from $\sum_{i=1}^N \lambda_i$ to $\sum_{i=1}^K \lambda_i$. Hence early-stage SGD is less noisy.

C.7 Curriculum time-to- ε bounds

Theorem C.10 (Two-stage time bound).

Run stage 1 in the PCA- K subspace for t_1 steps (step cost $T_{\text{step}}(K)$), yielding a loss gap $\Delta_1 \leq \rho_K^{t_1} \Delta_0$ with $\rho_K = 1 - \mu_K / L_K$. Then switch to full- N optimization until accuracy ε is reached. The total wall-clock time is bounded by

$$T_{\text{ours}}(\varepsilon; K, t_1) \leq t_1 T_{\text{step}}(K) + \kappa_N \log \frac{\Delta_1}{\varepsilon} \cdot T_{\text{step}}(N). \quad (\text{C5})$$

By contrast, the baseline (always full- N) obeys

$$T_{\text{base}}(\varepsilon) \leq \kappa_N \log \frac{\Delta_0}{\varepsilon} \cdot T_{\text{step}}(N). \quad (\text{C6})$$

Proof. Standard linear convergence for smooth strongly convex objectives implies $\mathcal{L}(w_t) - \mathcal{L}(w^*) \leq (1 - \mu/L)^t (\mathcal{L}(w_0) - \mathcal{L}(w^*))$. Apply this to stage 1 with (μ_K, L_K) and to stage 2 with (μ_N, L_N) , then sum wall-clock costs per step. \square

Corollary C.11 (When is the curriculum strictly faster).

Using $\Delta_1 = \rho_K^{t_1} \Delta_0$ in (C5), $T_{\text{ours}} < T_{\text{base}}$ whenever

$$\frac{t_1}{\kappa_N} \cdot \frac{T_{\text{step}}(K)}{T_{\text{step}}(N)} + \log \frac{\Delta_1}{\Delta_0} < 0. \quad (\text{C7})$$

Because $T_{\text{step}}(K) \ll T_{\text{step}}(N)$ by (C2) and $\log(\Delta_1/\Delta_0) = t_1 \log \rho_K < 0$, there is a wide range of (K, t_1) for which (C7) holds. If a bias floor $\Delta_{\text{bias}}(K)$ exists in the K -subspace (e.g., for squared loss this scales with $\sum_{i>K} \lambda_i$), pick t_1 so that $\Delta_1 \approx \max\{\Delta_{\text{bias}}(K), \varepsilon\}$.

Extension to S stages.

With $K_1 < \dots < K_{S-1} < K_S = N$, one obtains

$$T_{\text{ours}}(\varepsilon; \{K_s, t_s\}) \leq \sum_{s=1}^{S-1} t_s T_{\text{step}}(K_s) + \kappa_N \log \frac{(\prod_{s=1}^{S-1} \rho_{K_s}^{t_s}) \Delta_0}{\varepsilon} \cdot T_{\text{step}}(N), \quad (\text{C8})$$

so each stage multiplicatively shrinks the final log term.

C.8 Concrete numerical instantiation

Assume geometric spectral decay $\lambda_j = \lambda_1 \rho^{j-1}$ with $\rho = 0.95$, $N = 200$, squared loss, and ridge $\lambda = 0.01\lambda_1$. Then

$$\lambda_N = \lambda_1 \rho^{199} \approx 3.7 \times 10^{-5} \lambda_1, \quad \kappa_N = \frac{\lambda_1 + \lambda}{\lambda_N + \lambda} \approx \frac{1.01}{0.010037} \approx 100.6.$$

Pick $K = 20$ so $\lambda_K \approx 0.377\lambda_1$, giving $\kappa_K \approx \frac{1.01}{0.377+0.01} \approx 2.60$ and $T_{\text{step}}(K)/T_{\text{step}}(N) \approx K/N = 0.10$. Target $\varepsilon = 10^{-3}$, start from $\Delta_0 = 1$, and run stage 1 until $\Delta_1 = \delta = 5 \cdot 10^{-3}$. Then

$$t_1 \approx \kappa_K \log \frac{\Delta_0}{\delta} \approx 2.60 \log(200) \approx 13.8 \quad \Rightarrow \quad t_1 \cdot \frac{T_{\text{step}}(K)}{T_{\text{step}}(N)} \approx 1.38,$$

and stage 2 needs $t_2 \approx \kappa_N \log \frac{\delta}{\varepsilon} \approx 100.6 \log(5) \approx 162$ “full- N ” steps. Hence

$$T_{\text{ours}} \approx 163.4, \quad T_{\text{base}} \approx \kappa_N \log \frac{\Delta_0}{\varepsilon} \approx 100.6 \log(1000) \approx 694,$$

i.e., a $\sim 4.25 \times$ speedup. With an additional middle stage (e.g., $K_2 = 60$) that further reduces the gap before the full- N phase, total speedup robustly falls in the $2\text{--}7 \times$ range, matching experiments.

C.9 Why accuracy is preserved (and may improve)

Bias-variance accounting (squared loss).

If the Bayes linear predictor w^* is mostly supported on the top- K eigendirections, $\|(I - P_K)w^*\|_2^2 \leq \epsilon_{\text{bias}}$, then, with ridge parameter λ and noise variance σ^2 , the expected excess risk satisfies

$$\mathbb{E}[R(\hat{w}) - R(w^*)] \leq \epsilon_{\text{bias}} + \frac{\sigma^2}{M} \text{tr}(C(C + \lambda I)^{-1}).$$

Early PCA reduces the variance term via $\text{tr}(C_K(C_K + \lambda I)^{-1}) \leq \text{tr}(C(C + \lambda I)^{-1})$; the final stage returns to $K = N$, eliminating truncation bias. Thus accuracy is preserved (and sometimes improved through variance reduction and better initialization).

Continuation view for nonconvex models.

Early stages are better conditioned (smaller κ_K) and have lower SGD noise (Lemma C.9), smoothing the effective loss landscape. The optimizer finds a good basin at low dimension and then tracks it as K increases (a homotopy/continuation effect), reducing the risk of poor local minima.

C.10 Summary of the logical chain

1. **LFC pitfalls.** Convolutional low-pass induces spatial mixing and irreversible high-frequency loss (Lemmas C.2–C.3; [44]).
2. **PCA optimality.** PCA is the best linear rank- K compressor and is pointwise (no spatial mixing), with explicit tail error $\sum_{i>K} \lambda_i$ (Prop. C.4; [45]).
3. **Safe downsampling.** Per-PC low-pass + subsampling satisfies Shannon–Nyquist, so no aliasing; reconstructed spectra remain in the PCA subspace [43, 46].
4. **Cost drop.** Per-step cost shrinks by $\frac{K}{N} \frac{1}{d^2}$ (Lemma C.5).
5. **Faster convergence.** PCA improves conditioning and reduces SGD variance (Lemmas C.7–C.9), yielding tighter time-to- ε bounds with a staged schedule (Thm. C.10 and Cor. C.11).
6. **Accuracy preserved.** Final full- N stage removes truncation bias; early stages lower variance and provide better initialization.

■

References

- [1] He, Y., Tu, B., Liu, B., Li, J., Plaza, A.: Hsi-mformer: Integrating mamba and transformer experts for hyperspectral image classification. *IEEE Transactions on Geoscience and Remote Sensing* (2025)
- [2] El-Gabri, A.R., Aly, H.A., Ghoniemy, T.S., *et al.*: DLRA-Net: Deep local residual attention network with contextual refinement for spectral super-resolution. *Int. J. Comput. Vis.* **133**, 1499–1531 (2025) <https://doi.org/10.1007/s11263-024-02238-w>
- [3] Plaza, A., Benediktsson, J.A., Boardman, J.W., Brazile, J., Bruzzone, L., Camps-Valls, G., Chanussot, J., Fauvel, M., Gamba, P., Gualtieri, A., Marconcini, M., Tilton, J.C., Trianni, G.: Recent advances in techniques for hyperspectral image processing. *Remote Sens. Environ.* **113**(Supplement 1), 110–122 (2009) <https://doi.org/10.1016/j.rse.2007.07.028>
- [4] Landgrebe, D.: Hyperspectral image data analysis. *IEEE Signal processing magazine* **19**(1), 17–28 (2002)
- [5] Paoletti, M.E., Haut, J.M., Plaza, J., Plaza, A.: Deep learning classifiers for hyperspectral imaging: A review. *ISPRS Journal of Photogrammetry and Remote Sensing* **158**, 279–317 (2019)

- [6] Wang, T., Yan, Z., Li, J., *et al.*: Hyperspectral and multispectral image fusion with arbitrary resolution through self-supervised representations. *Int. J. Comput. Vis.* (2025) <https://doi.org/10.1007/s11263-025-02540-1>
- [7] Liu, Y., Dian, R., Li, S.: Low-rank transformer for high-resolution hyperspectral computational imaging. *Int. J. Comput. Vis.* **133**, 809–824 (2025) <https://doi.org/10.1007/s11263-024-02203-7>
- [8] Wang, Y., Yue, Y., Lu, R., Han, Y., Song, S., Huang, G.: Efficienttrain++: Generalized curriculum learning for efficient visual backbone training. *IEEE Transactions on Pattern Analysis and Machine Intelligence* **46**(12), 8036–8055 (2024)
- [9] Brown, T., Mann, B., Ryder, N., Subbiah, M., Kaplan, J.D., Dhariwal, P., Neelakantan, A., Shyam, P., Sastry, G., Askell, A., *et al.*: Language models are few-shot learners. *Advances in neural information processing systems* **33**, 1877–1901 (2020)
- [10] Devlin, J., Chang, M.-W., Lee, K., Toutanova, K.: Bert: Pre-training of deep bidirectional transformers for language understanding. In: *Proceedings of the 2019 Conference of the North American Chapter of the Association for Computational Linguistics: Human Language Technologies, Volume 1 (long and Short Papers)*, pp. 4171–4186 (2019)
- [11] He, K., Chen, X., Xie, S., Li, Y., Dollár, P., Girshick, R.: Masked autoencoders are scalable vision learners. In: *Proceedings of the IEEE/CVF Conference on Computer Vision and Pattern Recognition*, pp. 16000–16009 (2022)
- [12] Li, F., Zhang, H., Liu, S., Guo, J., Ni, L.M., Zhang, L.: Dn-detr: Accelerate detr training by introducing query denoising. In: *Proceedings of the IEEE/CVF Conference on Computer Vision and Pattern Recognition*, pp. 13619–13627 (2022)
- [13] Zoph, B., Ghiasi, G., Lin, T.-Y., Cui, Y., Liu, H., Cubuk, E.D., Le, Q.: Rethinking pre-training and self-training. *Advances in neural information processing systems* **33**, 3833–3845 (2020)
- [14] Romero, J., Yin, J., Laanait, N., Xie, B., Young, M.T., Treichler, S., Starchenko, V., Borisevich, A., Sergeev, A., Matheson, M.: Accelerating collective communication in data parallel training across deep learning frameworks. In: *19th USENIX Symposium on Networked Systems Design and Implementation (NSDI 22)*, pp. 1027–1040 (2022)
- [15] Wang, Z.-Q., Wang, D.: A joint training framework for robust automatic speech recognition. *IEEE/ACM Transactions on Audio, Speech, and Language Processing* **24**(4), 796–806 (2016)

- [16] Su, Q., Huang, R., He, H.: Heterogeneous multi-agent deep reinforcement learning for eco-driving of hybrid electric tracked vehicles: A heuristic training framework. *Journal of Power Sources* **601**, 234292 (2024)
- [17] Yu, X., Gao, Z., Xiong, Z., Zhao, C., Yang, Y.: Ddpg-adaptconfig: A deep reinforcement learning framework for adaptive device selection and training configuration in heterogeneity federated learning. *Future Generation Computer Systems* **163**, 107528 (2025)
- [18] Wang, X., Chen, Y., Zhu, W.: A survey on curriculum learning. *IEEE transactions on pattern analysis and machine intelligence* **44**(9), 4555–4576 (2021)
- [19] Zhu, H., Xie, W., Mu, Y., Xu, J., Wang, F.L., Qu, Y., Hao, T.: A new semi-supervised fuzzy k-means clustering method with dynamic adjustment and label discrimination. *Neural Computing and Applications* **36**(9), 4709–4725 (2024)
- [20] Hirano, Y., Okada, S., Komatani, K.: Recognizing social signals with weakly supervised multitask learning for multimodal dialogue systems. In: *Proceedings of the 2021 International Conference on Multimodal Interaction*, pp. 141–149 (2021)
- [21] Xu, J., Ma, X., Zhang, L., Zhang, B., Chen, T.: Push-and-pull: A general training framework with differential augmentor for domain generalized point cloud classification. *IEEE Transactions on Circuits and Systems for Video Technology* **34**(8), 7165–7175 (2024)
- [22] Calin, M.A., Calin, A.C., Nicolae, D.N.: Application of airborne and spaceborne hyperspectral imaging techniques for atmospheric research: Past, present, and future. *Applied Spectroscopy Reviews* **56**(4), 289–323 (2021)
- [23] Yan, H.Y., Zheng, R.Z., Boehm, B.B., Shaga, S.S., Black, D.B., Russell, R.R., Kursun, O.K.: Cloudpatch-7 hyperspectral dataset (2024)
- [24] He, K., Zhang, X., Ren, S., Sun, J.: Deep residual learning for image recognition. In: *Proceedings of the IEEE Conference on Computer Vision and Pattern Recognition*, pp. 770–778 (2016)
- [25] Todi, A., Narula, N., Sharma, M., Gupta, U.: Convnext: A contemporary architecture for convolutional neural networks for image classification. In: *2023 3rd International Conference on Innovative Sustainable Computational Technologies (CISCT)*, pp. 1–6 (2023). IEEE
- [26] Hampali, S., Sarkar, S.D., Rad, M., Lepetit, V.: Keypoint transformer: Solving joint identification in challenging hands and object interactions for accurate 3d pose estimation. In: *Proceedings of the IEEE/CVF Conference on Computer Vision and Pattern Recognition*, pp. 11090–11100 (2022)
- [27] Wang, J., Gao, F., Dong, J., Du, Q.: Adaptive dropblock-enhanced generative

adversarial networks for hyperspectral image classification. *IEEE Transactions on Geoscience and Remote Sensing* **59**(6), 5040–5053 (2020)

[28] Varahagiri, S., Sinha, A., Dubey, S.R., Singh, S.K.: 3d-convolution guided spectral-spatial transformer for hyperspectral image classification. In: 2024 IEEE Conference on Artificial Intelligence (CAI), pp. 8–14 (2024). IEEE

[29] Chen, N., Fang, L., Xia, Y., Xia, S., Liu, H., Yue, J.: Spectral query spatial: Revisiting the role of center pixel in transformer for hyperspectral image classification. *IEEE Transactions on Geoscience and Remote Sensing* **62**, 1–14 (2024)

[30] Xu, Y., Wang, D., Zhang, L., Zhang, L.: Dual selective fusion transformer network for hyperspectral image classification. *Neural Networks* **187**, 107311 (2025)

[31] Ravikumar, A., Rohit, P., Nair, M.K., Bhatia, V.: Hyperspectral image classification using deep matrix capsules. In: 2022 International Conference on Data Science, Agents & Artificial Intelligence (ICDSAAI), vol. 1, pp. 1–7 (2022). IEEE

[32] Wu, Y., Hu, D., Wu, M., Hu, X.: A numerical-integration perspective on gaussian filters. *IEEE transactions on signal processing* **54**(8), 2910–2921 (2006)

[33] Krishnan, S.R., Seelamantula, C.S.: On the selection of optimum savitzky-golay filters. *IEEE transactions on signal processing* **61**(2), 380–391 (2012)

[34] Chan, T.F., Osher, S., Shen, J.: The digital tv filter and nonlinear denoising. *IEEE Transactions on Image processing* **10**(2), 231–241 (2001)

[35] Mao, A., Mohri, M., Zhong, Y.: Cross-entropy loss functions: Theoretical analysis and applications. In: International Conference on Machine Learning, pp. 23803–23828 (2023). pmlr

[36] Shi, W., Gong, Y., Tao, X., Zheng, N.: Training dcnn by combining max-margin, max-correlation objectives, and correntropy loss for multilabel image classification. *IEEE transactions on neural networks and learning systems* **29**(7), 2896–2908 (2017)

[37] Liu, L., Qi, H.: Learning effective binary descriptors via cross entropy. In: 2017 IEEE Winter Conference on Applications of Computer Vision (WACV), pp. 1251–1258 (2017). IEEE

[38] Guan, L.: Weight prediction boosts the convergence of adamw. In: Pacific-Asia Conference on Knowledge Discovery and Data Mining, pp. 329–340 (2023). Springer

[39] Zhang, Y., Chen, C., Li, Z., Ding, T., Wu, C., Kingma, D.P., Ye, Y., Luo, Z.-Q., Sun, R.: Adam-mini: Use fewer learning rates to gain more. arXiv preprint arXiv:2406.16793 (2024)

- [40] Gower, R.M., Loizou, N., Qian, X., Sailanbayev, A., Shulgin, E., Richtárik, P.: Sgd: General analysis and improved rates. In: International Conference on Machine Learning, pp. 5200–5209 (2019). PMLR
- [41] Wang, Y., Hu, X., Hu, Y., *et al.*: Boosting domain generalization in remote sensing image segmentation via style mapping and general prototypical contrast. *Int. J. Comput. Vis.* (2025) <https://doi.org/10.1007/s11263-025-02568-3>
- [42] Fu, Y., Lam, A., Sato, I., *et al.*: Adaptive spatial-spectral dictionary learning for hyperspectral image restoration. *Int. J. Comput. Vis.* **122**, 228–245 (2017) <https://doi.org/10.1007/s11263-016-0921-6>
- [43] Gonzalez, R.C., Woods, R.E.: *Digital Image Processing*, 3rd edn. Prentice Hall, Upper Saddle River, NJ (2009)
- [44] Bracewell, R.N.: *The Fourier Transform and Its Applications*, 3rd edn. McGraw-Hill, New York (1999)
- [45] Jolliffe, I.T.: *Principal Component Analysis*, 2nd edn. Springer, New York (2002)
- [46] Shannon, C.E.: Communication in the presence of noise. *Proceedings of the IRE* **37**(1), 10–21 (1949) <https://doi.org/10.1109/JRPROC.1949.232969>
- [47] Chang, C.-I.: *Hyperspectral Imaging: Techniques for Spectral Detection and Classification*. Kluwer Academic / Plenum Publishers, New York (2003)
- [48] Schowengerdt, R.A.: *Remote Sensing: Models and Methods for Image Processing*, 3rd edn. Academic Press, Burlington, MA (2006)